

External Compton Radiation from Rapid Nonthermal Flares in Blazars

Andrei Sokolov¹ and Alan P. Marscher

*Institute for Astrophysical Research, Boston University, 725 Commonwealth Avenue,
Boston, MA 02215, USA*

asokolov@uclan.ac.uk, marscher@bu.edu

ABSTRACT

In this paper we extend our approach to modeling multifrequency emission variability from blazars to include external-radiation Compton (ERC) emission and electron energy losses from inverse Compton scattering of seed photons originating outside the jet. We consider seed-photon emission from a dusty molecular torus and the broad line region (BLR) surrounding the central engine. We establish constraints on the properties of the molecular torus and BLR under which synchrotron self-Compton (SSC) emission dominates such that the results obtained in our previous paper are applicable. The focus of this study is on relative time delays between the light curves observed at different frequencies. For definiteness, we consider emission resulting from a collision between relativistic shocks, but the results apply more generally to conditions involving acceleration of relativistic electrons and/or magnetic field amplification at any type of front. Unlike SSC emission, ERC flares involving a constant field of seed photons are not delayed by light travel time of the seed photons. The main cause of delays is from radiative energy losses, which result in frequency stratification behind the front and quench the flare first at the highest frequencies, progressing to lower frequencies as time advances. However, if the spectrum of electrons injected at the shock front is characterized by a relatively high value of the minimum energy (a Lorentz factor $\gamma_{min} \sim 100$ is sufficient), the ERC flare in the X-ray band can be delayed and may even peak after the injection has ceased. This effect is strongly frequency dependent, with a longer lag at lower frequencies and an X-ray spectral index that changes rapidly from positive (inverted spectrum) to steep values.

Subject headings: galaxies: active — galaxies: jets — radiation mechanisms: nonthermal

¹present address: Center for Astrophysics, University of Central Lancashire, Preston PR1 2HE, UK

1. Introduction

In Sokolov, Marscher, & McHardy (2004, hereafter Paper I), we introduced a model of blazar variability designed to study rapid flares resulting from particle acceleration at a shock front. The case considered involved a collision between relativistic shocks, but the effects incorporated, light-travel delays and energy/frequency stratification, are of general importance. The primary goal of that study was to establish the conditions for relative delays between synchrotron and synchrotron self-Compton (SSC) flares at different frequencies. We found that the SSC emission can be strongly affected by light travel time of the synchrotron seed photons, which can result in a considerable delay of the SSC flares in the X-ray band with respect to synchrotron variability at lower frequencies. In the present paper, we consider external sources of the seed photons that are scattered to high energies by the relativistic electrons heated at the front.

The current unified scheme of active galactic nuclei (Antonucci 1993) includes a source of obscuration that shields the emission from the region within $\sim 0.1\text{--}10$ pc of the central black hole when observed at large viewing angles. This obscuration is usually assumed to be provided by a dusty molecular torus that surrounds the innermost nuclear region. The dust in the inner portions of the torus facing the central continuum source is heated to temperatures $T \sim 1000$ K and emits infrared radiation roughly as a blackbody. In addition, reverberation studies of broad emission lines (Peterson 1993) suggest the presence of a clumpy broad emission line region (BLR) that consists of ionized clouds concentrated within $\sim 0.1L_{uv,42}^{1/2}$ pc of the black hole, where $L_{uv,42}$ is the UV spectral luminosity normalized by $10^{42} \text{ erg s}^{-1} \text{ \AA}^{-1}$. The combined BLR emission and blackbody radiation from the torus permeate the jet on parsec scales, providing a potentially significant source of seed photons, alongside the synchrotron seed photons produced by the jet plasma itself (e.g., see Błażejowski et al. 2000).

In the rest frame of the emitting plasma, radiation from the torus and BLR depends on location of the emission region in the jet and its bulk Lorentz factor Γ'_p . Radiation from the torus is in general expected to be Doppler boosted in the plasma rest frame. This results in stronger dependence of the ERC emission on Γ'_p compared with the SSC emission, whose seed radiation is produced in the rest frame of the plasma. However, this behavior can be modified by the effects of electron energy losses from ERC radiation which, if dominant, limit the spatial extent of the emitting plasma in an energy-dependent manner, leading to frequency stratification of the emission.

In this paper, we investigate the broadband features of the ERC emission during flares under different assumptions about 1) properties of the molecular torus, 2) location in the

jet where the flare occurs, and 3) the value of Γ'_p of the emitting plasma. As in Paper I, we concentrate on the study of relative delays between flares at different frequencies and the features that can be used to distinguish among different emission mechanisms. An additional goal of this study is to define the properties of the molecular torus and the BLR under which the results obtained in Paper I are valid. There we assumed that the ERC emission provides a negligible contribution compared with the SSC radiation at the frequencies of interest, and that the energy losses of electrons are dominated by synchrotron emission.

2. External Compton Model

The inclusion of ERC radiation in our model of variability introduces a new component of high-energy emission. It can also change the overall structure of the emission region and, hence, affect synchrotron and SSC radiation if the energy losses of electrons are dominated by scattering of external photons. In this case the decay time of electrons will be reduced compared with the case of pure synchrotron losses, which leads to changes in flux levels and values of critical frequencies, such as the break frequency. The details depend on the structure and properties of the sources of external emission, which we describe in this section.

As in Paper I, here we concentrate on the study of rapid variability on time scales ~ 1 day. We adopt the assumptions about geometry and excitation structure of the emitting volume made in Paper I. We ignore the expansion of the emission region, which is assumed to be a cylinder oriented along the jet. We assume that the size of the emitting volume is small compared to the sizes of and distances to the external sources of emission. Then we can assume that the external radiation is homogeneous throughout the emitting plasma, albeit highly anisotropic. The structure and location of the molecular torus and the BLR, as well as the location of the emitting plasma in the jet, determine the angular dependence of external emission. This anisotropy is further amplified by relativistic aberration and Doppler boosting or de-boosting in the rest frame of the plasma. For simplicity we assume that external radiation is static during the flare.

The properties of the putative dusty torus in the nucleus of an active galaxy are poorly known. In particular, despite what its name implies, the geometrical shape and size of this structure in a quasar or BL Lac object are poorly constrained. According to one model (Elvis 2000), the obscuration is provided by a conical outflow of the material from the accretion disk. Recent interferometric observations of the nucleus of NGC 1068 (Jaffe et al. 2004) reveal the presence of warm dust at temperature $T \sim 300$ K in a structure ~ 2.1 pc in size, surrounding a smaller, warmer ($T > 800$ K) structure of size ~ 0.7 pc. The mass of the black hole in NGC 1068 is $1.4 \times 10^7 M_\odot$ according to VLBI measurements of water maser emission

(Greenhill & Gwinn 1997). For quasars and BL Lac objects harboring more massive black holes, one should expect the size of the torus to scale accordingly.

Fig. 1 illustrates the geometry and size of the molecular torus in relation to the position of the emitting blob of plasma in the jet for a representative set of assumptions about the external sources of seed emission and the location of the radiating plasma. The torus is characterized by semi-opening angle θ_{op} and radius r_{tor} . We assume that the emission from the torus is dominated by dust that radiates as a black body at temperature T , so that the intensity of emission from the torus is

$$I'_{\nu'}(\theta') = \mathcal{B}_{\nu'}(T), \quad \text{for } \theta'_{min} < \theta' < \theta'_{max}, \quad (1)$$

where $\mathcal{B}_{\nu'}(T)$ is the Planck function. Here and below, the primed quantities associated with the emitting plasma are given in the rest frame of the host galaxy, whereas unprimed quantities are reserved for use in the plasma rest frame (this convention follows the one adopted in Paper I). We only take into account the emission from the portion of the torus that faces the central continuum source. However, the details of this approach are not crucial to the final results. The only essential parameters are the angle θ'_{min} , which determines the maximum Doppler boosting, and the dust temperature T .

The BLR can be represented by a uniform spherical source of emission at a fiducial frequency ν'_{blr} . The integrated intensity of the incident emission from the BLR is given by

$$I'(\theta') = \frac{L_{blr}/(4\pi)}{\frac{4}{3}\pi r_{blr}^3} \Delta r(\theta'), \quad \text{for } \theta'_{blr} < \theta' < 180^\circ, \quad (2)$$

where r_{blr} is the radius of the BLR, $\Delta r(\theta')$ is the geometric thickness of the BLR in a given direction, $\theta'_{blr} = \pi - \arcsin(r_{blr}/z_p)$, and L_{blr} is the BLR luminosity, which can be estimated from observations if the distance to the blazar is known. Again, as in the case of the molecular torus, the angle θ'_{blr} and the BLR luminosity L_{blr} are the only essential parameters.

The UV spectral luminosity of 3C 273 can be estimated as $L_{uv,42} \approx 2$ (von Montingy et al. 1997), which gives the size of the BLR region as ~ 0.14 pc. Although the size of the torus in 3C 273 is unknown, it is reasonable to expect that it is at least 10 pc. For the calculations reported in this paper, we assume that the location of the emitting plasma $z_p \approx r_{tor}$. Under this condition the contribution of the BLR region to the seed photon field is negligible since BLR emission is significantly de-boosted by relativistic Doppler effects. We therefore neglected the contribution from the BLR in the reported results. However, the role of the BLR would increase sharply if the event that causes the flare were to occur closer to the central engine and, hence, closer to or even within the BLR.

The plasma that produces variable emission during a flare moves down the jet at a relativistic speed $v'_p = c\beta'_p$, with corresponding Lorentz factor Γ'_p . The Doppler effect and

relativistic aberration cause the intensity of external radiation to be highly anisotropic in the plasma rest frame. The direction of incoming radiation is modified by relativistic aberration according to

$$\mu = (\mu' - \beta'_p)/(1 - \beta'_p\mu'), \quad (3)$$

where $\mu' = -\cos\theta'$ and θ' is the angle of propagation of the incident photons relative to the line of sight; μ is the corresponding quantity in the plasma rest frame. The spectral intensity of incident emission from the molecular torus is transformed according to $I_\nu(\mu) = \delta^3 I'_{\nu'}(\mu')$, where the Doppler factor $\delta = \Gamma'_p(1 - \beta'_p\mu')$ and $\nu = \delta\nu'$, while the expression for transforming incident integral intensity is $I(\mu) = \delta^4 I'(\mu')$. Thus, for the parameters used in Fig. 1, the maximum Doppler factor for the emission from the torus $\delta_{max} \approx \Gamma'_p$.

Once the intensity as a function of direction is known, one can determine the value of the external radiation energy density in the rest frame of the emitting plasma by integrating over all allowed incident directions and over the black-body spectrum. The external radiation energy density from three different models of the molecular torus is presented in Fig. 2 as a function of position of the emitting plasma in the jet. The position of the emitting plasma is a free parameter of the model. It does not change during the calculations, but adopting a different value may affect the results of the simulations considerably. The energy density of the magnetic field in the plasma rest frame $u_B = B^2/(8\pi)$, where the magnetic field strength as a function of position z_p along the jet is given by $B(z_p) = B_0 z_0/z_p$. It can be seen that the energy density of emission from the torus exceeds that of the magnetic field for $z_p \lesssim 40$ pc when the magnetic field B_0 is within half an order of magnitude of our adopted value of 0.4 G.

The expression for the energy density of blackbody radiation in the rest frame of the plasma can be integrated to produce the following approximate expression:

$$u_{rad} \approx \frac{2\pi}{c} \sigma T^4 \frac{\delta_{max}^3}{3\Gamma'_p}, \quad (4)$$

where σ is the Stefan-Boltzmann constant. When the location of emitting plasma $z_p \approx r_{tor}$, one has $\theta'_{min} \approx 90^\circ$ and the corresponding $\mu' \approx 0$. Under these conditions the ratio of the external radiation and magnetic energy densities has a simple dependence on the physical parameters:

$$u_{rad}/u_B \approx 30 \left(\frac{T}{1200 \text{ K}} \right)^4 \left(\frac{\Gamma'_p}{10} \right)^2 \left(\frac{B}{0.4 \text{ G}} \right)^{-2}. \quad (5)$$

It can be seen that moderate changes in the parameters can result in the case where magnetic energy density dominates and, therefore, energy losses of electrons are primarily due to synchrotron (or SSC) emission. For $T = 800\text{K}$ and $B = 1\text{G}$, $u_{rad} \approx u_B$ if $\theta'_{min} \approx 90^\circ$. Unfortunately, no simple approximation is available for the dependence of u_{rad} on the location

of the emitting plasma z_p when it is different from $z_p \approx r_{tor}$. If the size of the torus is considerably larger than z_p , the angle $\theta'_{min} \approx \theta_{op}$, which generally results in a somewhat larger value of δ_{max} and, hence, even more pronounced dominance of u_{rad} over u_B . On the other hand, if $z_p > r_{tor}$, the contribution from the torus is diminished rapidly with increasing z_p . Since u_{rad} can exceed u_B when $z_p \lesssim r_{tor}$, it must in general be taken into account when considering electron energy losses, which can be expressed as $\dot{\gamma} = -\gamma^2/t_u$, where

$$t_u = \frac{7.73 \times 10^8 \text{ s}}{8\pi(u_B + u_{rad})}. \quad (6)$$

The formalism developed in Paper I can be recovered completely by substituting t_1 defined there with t_u . The ERC flux $F_\nu^E(t_{obs})$ as a function of time t_{obs} and frequency ν of observation can then be calculated by utilizing the same procedures that are employed in the SSC calculations.

3. Calculated Spectra and Light Curves

In this section, we present the results of simulations of ERC emission variability. We study both the broadband spectral variability (Figs. 3 and 4) and the light curves at several representative frequencies (Figs. 5 through 8) for two viewing angles: $\theta_{obs} = 0^\circ$ corresponding to the case when the line of sight coincides with the jet axis, and $\theta_{obs} = 90^\circ$ in the rest frame of the plasma, which maximizes superluminal motion and reduces to the small angle $\theta'_{obs} \sim 1/\Gamma'_p$ in the frame of the host galaxy. To characterize external emission we specify the bulk Lorentz factor of the emitting plasma $\Gamma'_p = 10$. All the results presented in this section are given in the rest frame of the emitting plasma.

We use the same input parameters for the emitting plasma as the ones employed in the companion SSC calculations. The parameters describing external sources of emission, as well as the bulk speed of the emitting plasma, are chosen such that the ERC flux dominates over the SSC radiation at the frequencies of interest. This corresponds to the external radiation energy density in the plasma rest frame exceeding the energy density of the magnetic field. This affects the decay time of electrons and, therefore, the synchrotron and SSC emission variability. The comparison between the SSC and ERC spectral energy distribution (SED) at high frequencies is shown in Fig. 9. Scattered photons from the molecular torus dominate at frequencies above 10^{16} Hz in the calculations. Scattered BLR radiation is not shown, since it provides a negligible fraction of the external photons because of severe Doppler de-boosting.

3.1. Spectral Evolution

Figs. 3 and 4 show a sequence of SEDs from the forward-shock region (see Paper I) at different times normalized by the apparent crossing time t_{ac} . The latter quantity is defined in terms of the size of the excitation zone, which extends over a span $2R$ across and H along the jet, the speed of the shock in the plasma rest frame v , and the viewing angle: $t_{ac} = [(c/v) - 1]H/c$ for $\theta_{obs} = 0^\circ$ and $t_{ac} = 2R/c + H/v$ for $\theta_{obs} = 90^\circ$ (for more details see Paper I). The spectral features of the ERC emission depend on the characteristic frequency of the infrared photons from the torus at temperature T : $\nu_{tor} \sim 3kT/h$. The ERC spectrum can be characterized by three critical frequencies. (1) The spectrum drops off exponentially above frequency $\nu_{e,max}(t=0) \approx 4\gamma_{max}^2(t=0)\delta_{max}\nu_{tor}$ until $t = t_{ac}$, after which the drop-off frequency begins to fall quickly due to the sharp decrease in the maximum value of the Lorentz factor of electrons in the plasma owing to radiative cooling. (2) The turn-over frequency of the SED, $\nu_{e,t} \approx 4\gamma_{min}^2(t_{obs})\delta_{max}\nu_{tor}$, decreases during the flare as γ_{min} declines from the initial value, $\gamma_{min}(t=0)$. The value of the turn-over frequency at the crossing time t_{ac} depends on the energy loss rate of electrons, which in turn depends on the bulk speed of the plasma if ERC losses are dominant. (3) A break frequency $\nu_{e,b}$ is well defined in the case of the ERC spectrum since the seed photon SED is nearly monochromatic. It is found by solving the equation $t_\nu^E = \min\{t_{obs}, t_{ac}\}$ for ν , where the decay time at frequency ν is defined as

$$t_\nu^E = t_u \sqrt{\frac{4\delta_{max}\nu_{tor}}{\nu}}. \quad (7)$$

Above the break frequency the decay of the emitting electrons is high enough that the actual volume of plasma that contributes to the observed flux is smaller than that defined by the extent of the excitation zone through the parameters R and H . Because of this, the slope of the ERC spectrum steepens by $1/2$ above the break frequency due to the relations $t_\nu^E \propto \nu^{-1/2}$ and $F_\nu^E \propto j_\nu^E t_\nu^E$ (see Marscher & Gear 1985).

3.2. Time delays

As far as the time delays are concerned, the ERC flares at different frequencies are affected by the geometry of the excitation region and by electron energy stratification in the same manner as synchrotron and SSC emission. However, certain aspects of the ERC emission variability are markedly different. Below, we describe the general features of the ERC flares and the unique characteristics that distinguish them from synchrotron and SSC flares.

The ERC light curves for the viewing angle $\theta_{obs} = 0^\circ$ are presented in Fig. 5 for $\gamma_{min} =$

100 and Fig. 6 for $\gamma_{min} = 10$. The frequencies were chosen around the break frequency at the crossing time so that the resulting profiles are roughly symmetric. At higher frequencies the profile of a flare is expected to have a flat top, which is evident in the light curve at frequency $\nu = 2.5 \times 10^{18}$ Hz (dot-dashed curves). The decay time of scattering electrons that provide the dominant contribution to the observed ERC flux is smaller than the apparent crossing time. The light curves at lower frequency, $\nu = 4 \times 10^{17}$ Hz, are symmetric because the decay time of electrons matches the apparent crossing time (dashed curves). All light curves peak at the crossing time in the case of $\gamma_{min} = 10$. This is to be expected since the seed emission from the torus is constant during the flare, unlike the seed emission in the SSC model. However, in the case of $\gamma_{min} = 100$ the light curve at $\nu = 4 \times 10^{17}$ Hz peaks after the crossing time. It is also evident that the spectral index of the ERC emission is positive at the beginning of the flare when $\gamma_{min} = 100$. Positive values of the spectral index indicate that the light curves are observed at frequencies below the turn-over frequency, which depends on γ_{min} .

This unusual time delay of the ERC light curve can be understood as follows. The frequencies at which this delay can be observed are below the turn-over frequency at the crossing time. This means that the optimum Lorentz factors of scattering electrons that could provide the dominant contribution to the observed flux at these frequencies are below the minimum Lorentz factor of the injected electrons. As the flare progresses, the minimum Lorentz factor of the evolving electrons will eventually drop to the optimum values for the emission at frequencies below the turn-over frequency. However, if the initial γ_{min} is high enough, the optimum value might only be reached after the crossing time. In this case, the ERC emission at the frequency that corresponds to this optimum value will continue to grow even after time t_{ac} when the shock front exits the excitation region and the acceleration of electrons stops. This phenomenon should not affect the SSC flares in the same fashion since seed photons from a broad range of frequencies contribute equally to the SSC emission at a given frequency of observation. The frequencies at which electrons with Lorentz factor γ_{min} emit synchrotron radiation are generally lower than the synchrotron self-absorption frequency for realistic parameters. Therefore, synchrotron flares should not be expected to exhibit this effect, either.

The ERC light curves for the viewing angle $\theta_{obs} = 90^\circ$ are presented in Fig. 7 for $\gamma_{min} = 100$ and Fig. 8 for $\gamma_{min} = 10$. At a viewing angle of 90° the light curves at higher frequencies, defined by $t_\nu^E \lesssim t_{ac}$, peak at $\sim t_{ac}/2$ as a result of 1) rapid decay of electrons that dominate the observed emission at higher frequencies and 2) the circular geometry of the source along the line of sight. At lower frequencies defined by $t_\nu^E \gtrsim t_{ac}$, the maximum is closer to t_{ac} since this is when the emission fills the entire volume of the source. The mechanism that causes extra delay of the ERC emission, which was described above, affects

ERC light curves at any viewing angle, including $\theta_{obs} = 90^\circ$. However, when the viewing angle $\sim 90^\circ$ the effect is not as obvious since the delays due to the geometrical shape of the source and energy stratification are equally important.

In the calculations discussed here the parameters have been selected such that inverse Compton energy losses dominate over synchrotron losses, $u_{rad} \approx 30u_B$. This, in particular, means that the decay time of synchrotron emission is shorter than that calculated from synchrotron losses alone by a factor $\sim u_{rad}/u_B$. In Paper I we neglected external emission; the break frequency of the synchrotron spectrum was at $\sim 10^{12}$ Hz while the synchrotron self-absorption frequency $\sim 10^{10}$ Hz. The dominance of ERC losses in the present calculations shifts the break frequency of the synchrotron spectrum to $\sim 10^9$ Hz, which is less than the self-absorption frequency. Therefore, the synchrotron light curves at all frequencies of interest originate from a volume of the source that is limited by frequency stratification. These light curves are expected to peak at $\sim t_{ac}/2$ when $\theta_{obs} \sim 90^\circ$. In contrast, when $\theta_{obs} = 0^\circ$ the synchrotron flares at high frequencies (at which $t_\nu < t_{ac}$) are characterized by a quick rise, flat top, and equally rapid decay after the crossing time.

Comparing this behavior with that of the ERC light curves, one can assert that there must be a delay of about half the crossing time between the synchrotron flares and the ERC emission in the soft X-ray band (frequencies such that $t_\nu^E > t_{ac}$) for viewing angle $\theta_{obs} \sim 90^\circ$. The synchrotron flare should cease sharply before the peak of the ERC emission is reached if the viewing angle $\theta_{obs} = 0^\circ$. This implies that the parameters of the emission region and the external seed photon field are such that the break frequency of the synchrotron spectrum is below the frequency of observation (which can be verified by observing a rather steep synchrotron spectrum, with slope between -1 and -1.5). If this is not the case, smaller delays must be expected.

It should be noted that the presented results are independent of the size of the torus as long as the location of the emitting plasma in the jet z_p is adjusted by the same factor as the size of the torus r_{tor} . This ensures that the angles θ'_{min} and θ'_{max} are the same, which results in the same field of seed photons if the dust temperature is the same. On the other hand, if one keeps z_p constant then adoption of a larger torus results in amplification of the external seed photons and, consequently, more rapid decay of scattering electrons.

4. Discussion

The study that we have conducted allows one to distinguish between different emission mechanisms by means of the constraints placed on the magnitude of time delays between

flares and shapes of the light curves at different frequencies. At viewing angle $\theta_{obs} = 90^\circ$ in the rest frame of the emitting plasma, synchrotron and inverse Compton (both SSC and ERC) flares exhibit similar behavior in terms of time delays. The maximum time delay cannot exceed half the crossing time t_{ac} , which can crudely be equated with the duration of the flare when the light curves are symmetric. For this and other viewing angles, the flares must be asymmetric, with a quick rising part and long quasi-exponential decay if observed at frequencies significantly below the break frequency ν_b , whose value is different for each emission mechanism. The flares observed at or above the break frequency reflect the geometry of the source along the line of sight and are symmetric in our simulations because of the cylindrical geometry of the excitation volume.

Observing flares at zero viewing angle allows one to distinguish more clearly between emission mechanisms. The higher frequency synchrotron light curves should peak at exactly the crossing time, whereas the SSC and ERC flares in the X-ray band have an extra time delay and, thus, peak after the crossing time. For this viewing angle, the flares are symmetric if observed at or near the break frequency, whereas the flares will have a flat top at higher frequencies. In the case of the SSC emission, the delay is due to the light travel time of the synchrotron seed photons. The ERC light curve might show similar delay due to the decay of the minimum Lorentz factor of electrons if the initial value is large enough ($\gamma_{min} = 100$ at $t = 0$ proved sufficient in our simulations). If the initial $\gamma_{min} \ll 100$, no extra time delay of the ERC emission is possible. In addition, if the ERC emission exhibits an extra delay compared to the synchrotron variability at lower frequencies, the spectral index of the ERC emission must be positive for a significant fraction of the duration of the flare. This is because this extra delay is only possible for the ERC light curves at frequencies below the initial turn-over frequency of the SED. On the other hand, the spectral index of the SSC emission will be negative even at the beginning of the SSC flare because the turn-over frequency of the SSC spectrum is determined by the synchrotron self-absorption frequency, which is typically much lower than the characteristic frequency of dust emission, ν_{tor} .

Similar behavior of the ERC flares has been found by Sikora et al. (2001). These authors explained the delays that they found by appealing to the gradient in the magnetic field along the jet, which leads to a decrease in the critical frequency of synchrotron emission. In their model the flare is produced by a plasma in a geometrically thin shell energized by forward/reverse shocks produced following the collision between portions of the jet propagating with different relativistic speeds. In contrast with our model, these authors assume that the injection of relativistic electrons is uniform throughout the shell. They ascribe the time delays between ERC and synchrotron flares to gradients in magnetic field. Their modeling is thus suitable to more prolonged flares than the ones considered in this paper.

The results reported in Paper I are based on the assumption that the energy losses of electrons are dominated by synchrotron emission and that ERC emission is negligible compared to the SSC flux levels at the frequencies of interest. These assumptions are valid when the properties of the sources of external emission as well as the location of the emitting plasma in the jet are as in Fig. 10. Decreasing the size of the torus and/or placing the emitting plasma farther down the jet substantially decreases the Doppler boosting even if Γ'_p remains the same. For the parameters used in Fig. 10 the ERC losses of electrons are only a fraction of the synchrotron losses. Also, the SSC flux exceeds the ERC flux by a factor of at least a few at all frequencies and by several orders of magnitude near 10^{16} Hz (in the plasma rest frame), at which the SSC flare has been shown in Paper I to have an extra delay due to the travel time of the seed photons.

The results of simulations in the plasma rest frame can be transformed to the observer's frame according to the following expressions: $F_{\nu_*}^*(t_{obs}^*) = \delta_{obs}^3 (D_0/D^*)^2 F_\nu^E(t_{obs})$, $\nu_* = \delta_{obs}\nu/(1+z)$, and $t_{obs}^* = (1+z)t_{obs}/\delta_{obs}$, where the asterisk denotes quantities in the observer's frame, δ_{obs} is the Doppler factor determined by Γ'_p and the viewing angle, and z and D^* are the redshift and distance to the blazar (D_0 is the reference distance used in the simulations). This implies a particular dependence of the observed quantities on the bulk Lorentz factor of the emitting plasma. However, in the case where the energy losses of electrons are dominated by ERC emission, this dependence will be different due to energy stratification of the emitting volume. Indeed, if the frequency of observation is above the break frequency, the size of the actual emitting volume that contributes to the observed flux is smaller than the size of the excitation region caused by the shock collision. In this case the thickness of the emitting volume is determined by the decay time of the ERC emission:

$$t_\nu^E \propto \frac{\sqrt{\delta_{max}}}{u_{rad}} \propto \Gamma'_p \delta_{max}^{-2.5}. \quad (8)$$

This expression follows from the definition of the decay time plus Eq. (4). By applying the Doppler boosting formulas to the external emission, one can show that the ERC emission coefficient $j_\nu^E \propto \delta_{max}^{3+(s-1)/2} \Gamma_p'^{-1}$, where $-s$ is the slope of the injected power-law distribution of electron energies. By combining these two formulas, one finds for the ERC flux in the plasma rest frame $F_\nu^E \propto j_\nu^E t_\nu^E \propto \delta_{max}^{(s-2)/2}$. For $s = 2$ the ERC flux in the plasma rest frame does not depend on the bulk speed of the emitting plasma despite relativistic boosting of the incident emission, as one can see in Fig. 11. Similar reasoning applied to the SSC decay time gives $t_\nu^C \propto \Gamma_p'^3 \delta_{max}^{-3}$. The synchrotron emission that provides the seed photons for the SSC radiation is affected in a similar way, which results in $F_\nu^C \propto j_\nu^C t_\nu^C \propto \Gamma_p'^2 \delta_{max}^{-6}$ for the SSC flux above the break frequency, in the rest frame of the plasma. These modifications are due to internal structure of the emitting medium and, thus, cannot be reproduced by the homogeneous models such as Dermer et al. (1997); Sikora et al. (2001). The results reported

in Dermer et al. (1997), including the boosting formulas that give the dependence of observed flux on the Doppler factor of the emitting medium, should only apply to stationary emission or in a limited way to the flares observed at or below the break frequency. The break in the electron energy distribution used in these studies can only occur in a homogeneous medium with uniform and continuous injection of electrons, and is not applicable to flares generated by acceleration of electrons at shocks or any other type of front.

5. Conclusions

To expand the realm of the calculations of Paper I, we have conducted simulations of the external Compton emission generated by collisions of shocks in a relativistic jet in a blazar. We have considered the physical conditions under which the emission at high energies is dominated by either SSC or ERC emission. If the emitting region in the jet lies beyond the distance of the torus from the central engine, then SSC will dominate and the results of Paper I should be used to calculate the evolution of the high-energy spectrum. Otherwise, ERC will be more important because of substantial relativistic boosting of the external seed emission and the results of this paper are relevant.

For the case when ERC emission dominates, we have investigated the multifrequency light curves and determined that ERC flares at lower frequencies can incur an extra time delay due to the minimum Lorentz factor cut-off in the injected distribution of electrons. The simulations indicate that the spectral index of the ERC emission must be positive for at least half of the duration of the flare for such a delay to occur, which distinguishes it from a time delay of the SSC emission, which is characterized by a negative spectral index at all times. We have also found that if the energy losses of electrons are dominated by ERC emission, the dependence of the observed flux (synchrotron, SSC, and ERC) on the bulk speed of the emitting plasma is different from that expected in homogeneous models. In particular, there is no double boosting of the ERC emission, while the SSC flux might even decrease at higher values of the bulk Lorentz factor of the emitting plasma.

When the blazar is observed along the jet axis, flat tops are expected in light curves observed at frequencies sufficiently above the break frequency. If the flares are symmetric, it is possible for both SSC and ERC emission to peak in the soft X-ray band after the maximum of the synchrotron light curve. The value of the X-ray spectral index during the flare distinguishes between the SSC and ERC emission mechanism. The latter is characterized by more shallow or even positive spectral index. The delayed ERC emission indicates that the minimum Lorentz factor of the injected electrons is high enough so that the frequency of observation is at or below the turn-over frequency of the ERC spectrum. Otherwise, ERC

emission should peak at the same time as the synchrotron flare.

When superluminal apparent motion is observed in VLBI images, the viewing angle cannot be zero. In this case the behavior of the light curves is different; it is closer to that found for $\theta_{obs} = 90^\circ$. Synchrotron flares that peak at IR or optical frequencies precede the SSC and ERC flares in soft X-rays by $\Delta t \sim t_{ac}/2$ owing to frequency stratification.

This material is based on work supported by NASA grants NAG5-13074 and NNG04GO85G, as well as National Science Foundation grant AST-0406865.

REFERENCES

- Antonucci, R. 1993, *ARA&A*, 31, 473
- Błażejowski, M., Sikora, M., Moderski, R., & Madejski, G. M. 2000, *ApJ*, 545, 107
- Dermer, C. D., Sturmer, S. J., Schlickeiser, R. 1997, *ApJS*, 109, 103
- Elvis, M. 2000, *ApJ*, 545, 63
- Greenhill, L. J.; Gwinn, C. R. 1997, *Ap&SS*, 248, 261
- Jaffe, W. et al. 2004, *Nature*, 429, 47
- Korista, K. T. et al. 1995, *ApJS*, 97, 285
- Marscher, A. p., & Gear, W. K. 1985, *ApJ*, 298, 114
- Peterson, B. M. 1993, *PASP*, 105, 247
- Sikora, M., Błażejowski, M., Begelman, M. C.; Moderski, R. 2001, *ApJ*, 554, 1; erratum: 2001, *ApJ*, 561, 1154
- Sokolov, A., Marscher, A. P., & McHardy, I. 2004, *ApJ*, 613, 725 [Paper I]
- von Montigny, C., et al. 1997, *ApJ*, 483, 161

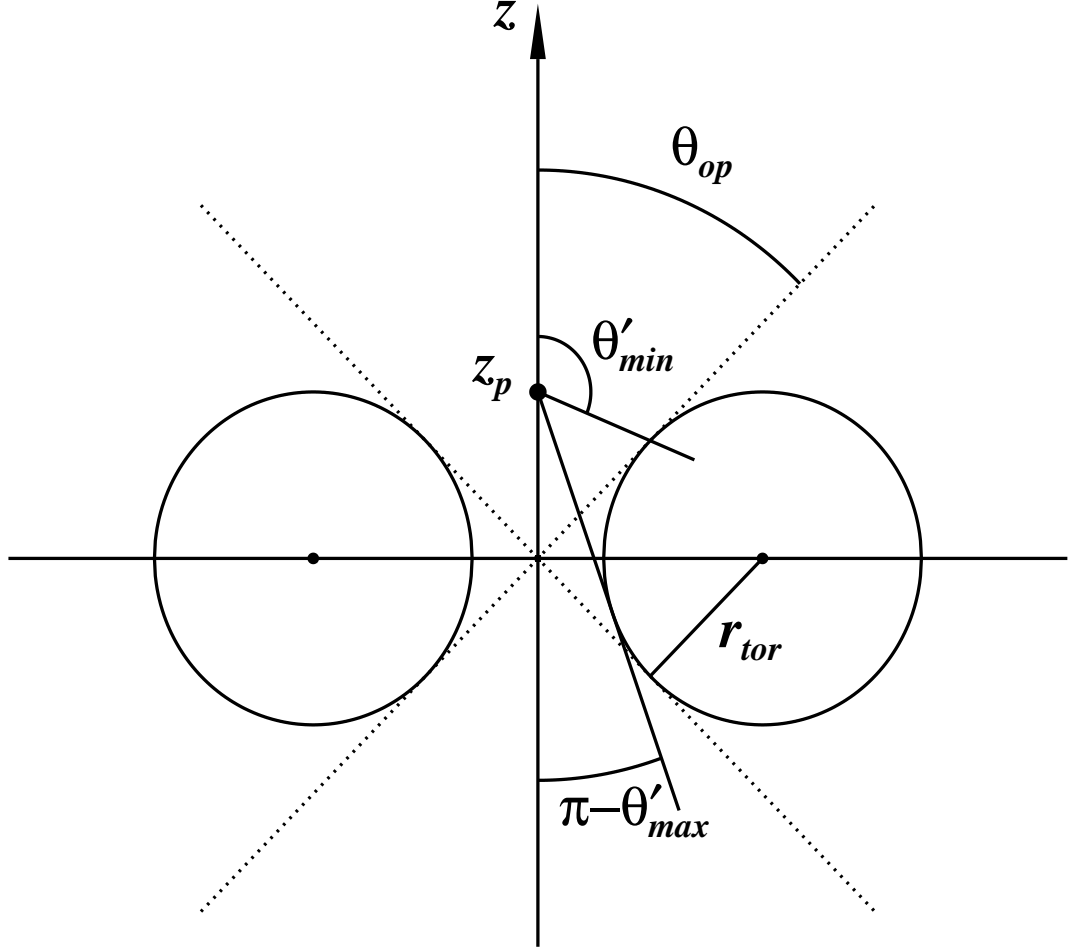


Fig. 1.— A schematic diagram of the central region of an active galaxy showing the location of the relativistic plasma in the jet at position z_p in relation to the molecular torus with semi-opening angle θ_{op} and radius r_{tor} . In this sketch, $\theta_{op} = 45^\circ$, and $r_{tor} = z_p$. The incident emission from the torus is assumed to be constrained between the minimum and maximum angles, θ'_{min} and θ'_{max} , respectively. Only a fraction of the torus that faces the center is assumed to be hot enough to contribute substantially to the seed photon field at z_p .

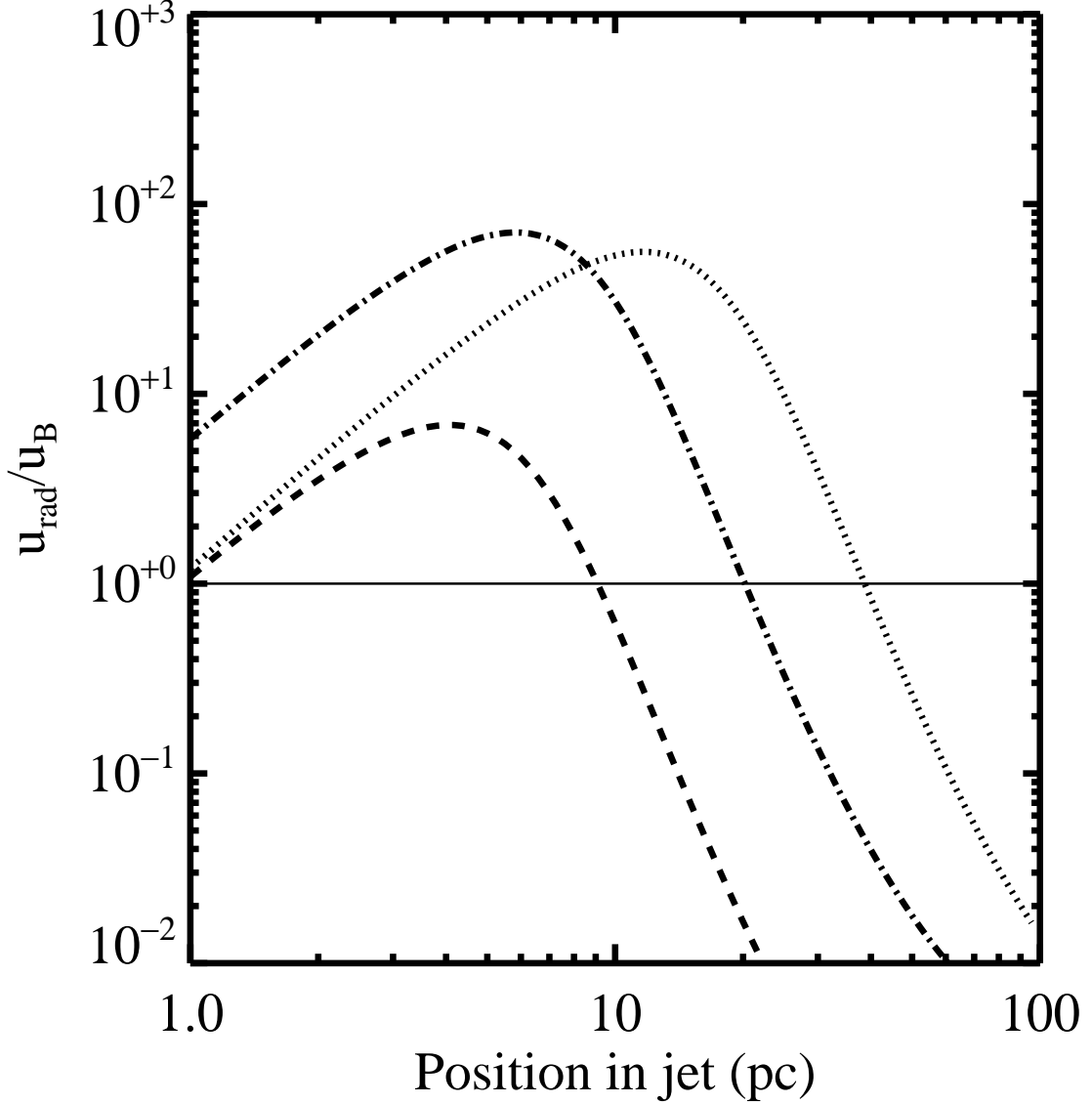


Fig. 2.— Ratio of the energy density of the external radiation field to that of the magnetic field for three models of the molecular torus, as a function of position of emitting plasma along the jet z_p , in the frame of the jet plasma for bulk Lorentz factor $\Gamma'_p = 10$. The semi-opening angle of the tori is 45° for all three models. The plot compares contributions from (1) moderately hot dust, $T = 800$ K, within a torus of smaller size, $r = 7.0$ pc (long-dashed curve), (2) the same but with larger size, $r = 20$ pc (dotted curve), and (3) a hotter torus with $T = 1200$ K and $r = 10$ pc (dot-dashed curve). The adopted rest-frame value of the magnetic field strength is $B = B_0 z_0 / z_p$, with $B_0 = 0.4$ G and $z_0 = 10$ pc.

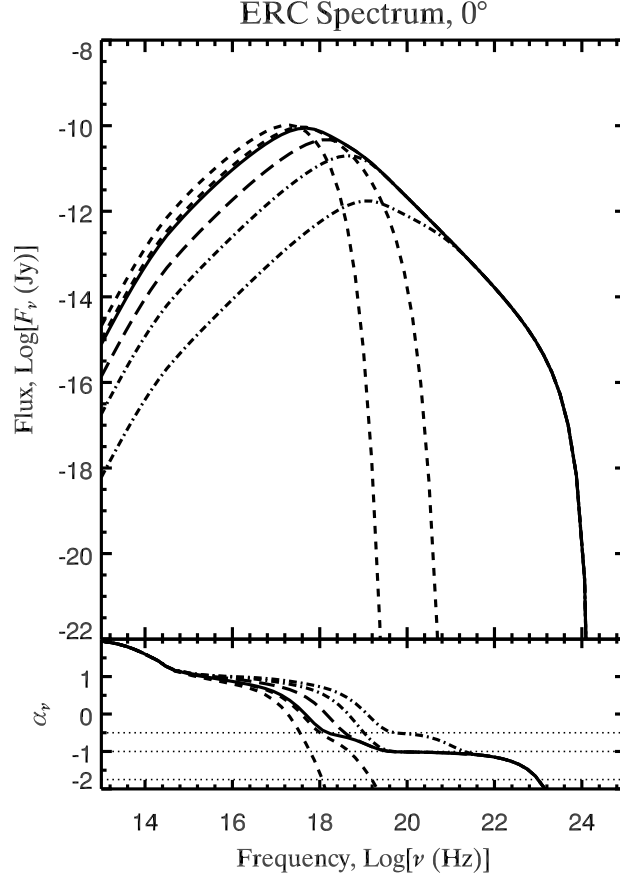


Fig. 3.— The evolution of the broadband external Compton spectrum for viewing angle $\theta_{obs} = 0^\circ$. The calculation for this and subsequent figures is carried out for an observer at rest relative to the emitting plasma. Only the contribution from the forward-shock region is considered. The individual spectra shown are for the following times t/t_{ac} : 0.02, 0.2 (dot-dashed), 0.5 (long dashed), 1.0 (solid), 1.1, 1.5 (short dashed). The bottom panel indicates the evolution of the spectral index α_ν , defined by $F_\nu(t_{obs}) \propto \nu^{\alpha_\nu}$. The following input parameters describing the shocked plasma were used: $R = H = 4 \times 10^6$ s, $v = 0.34c$, $B = 0.4$ G, $n = 10 \text{ cm}^{-3}$, $\gamma_{min} = 100$, $\gamma_{max} = 2 \times 10^4$, power-law electron energy distribution of slope $-s$ with $s = 2$, and fiducial distance $D_0 = 10^3$ Mpc. These are defined in the rest frame of the emitting plasma and identical to the ones used in Paper I. The emitting plasma is assumed to be located at $z_p = 10$ pc in the jet and moving downstream at Lorentz factor $\Gamma'_p = 10$. The external emission is characterized by the parameters used in Fig. 2, model (3).

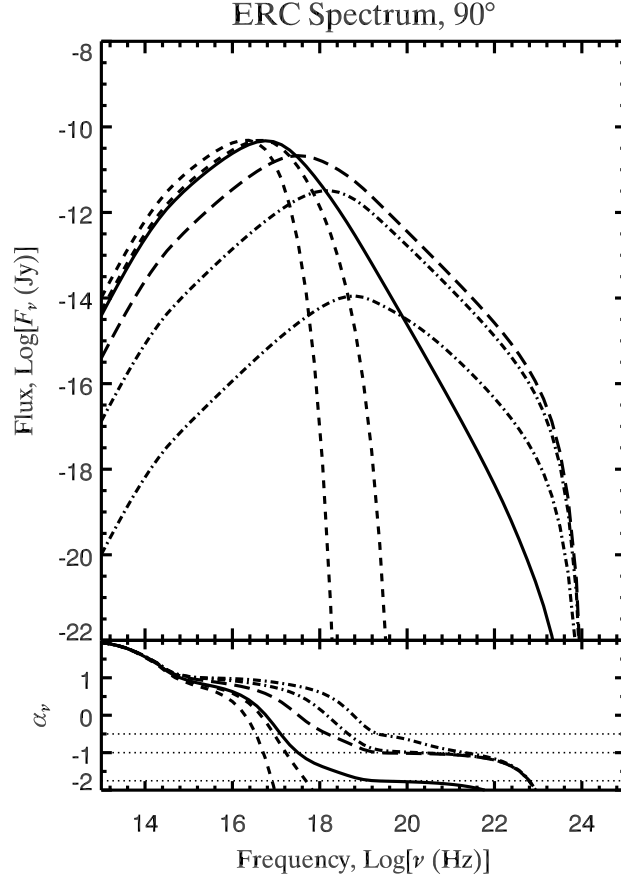


Fig. 4.— The same as in Fig. 3 but for a viewing angle of 90° in the rest frame of the emitting plasma, or $\sin^{-1}(1/\Gamma'_p)$ in the observer's frame.

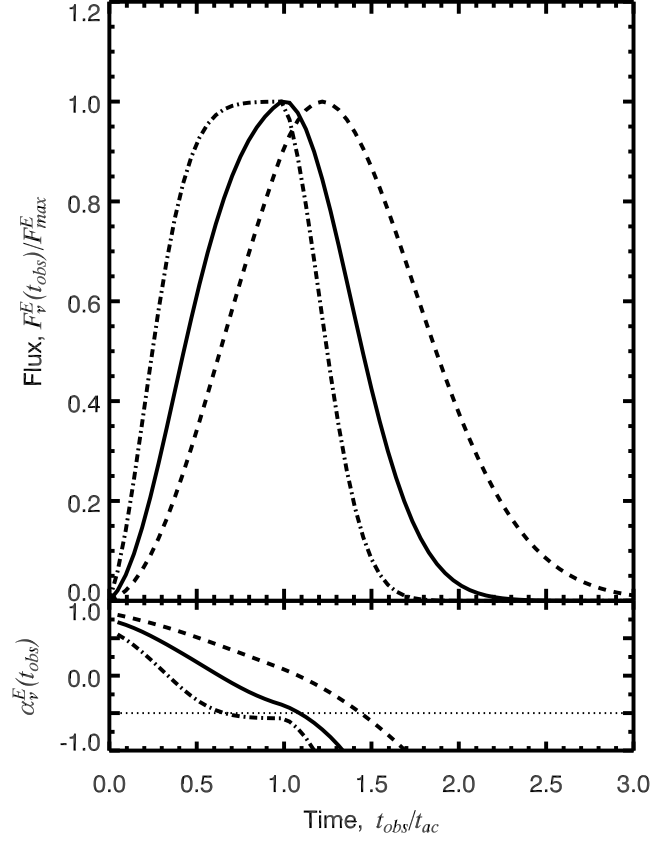


Fig. 5.— Normalized external Compton light curves for viewing angle $\theta_{obs} = 0^\circ$ at frequencies of 4×10^{17} Hz (dashed), 10^{18} Hz (solid), and 2.5×10^{18} Hz (dot-dashed). The time dependence of the spectral index for each light curve is shown in the lower panel.

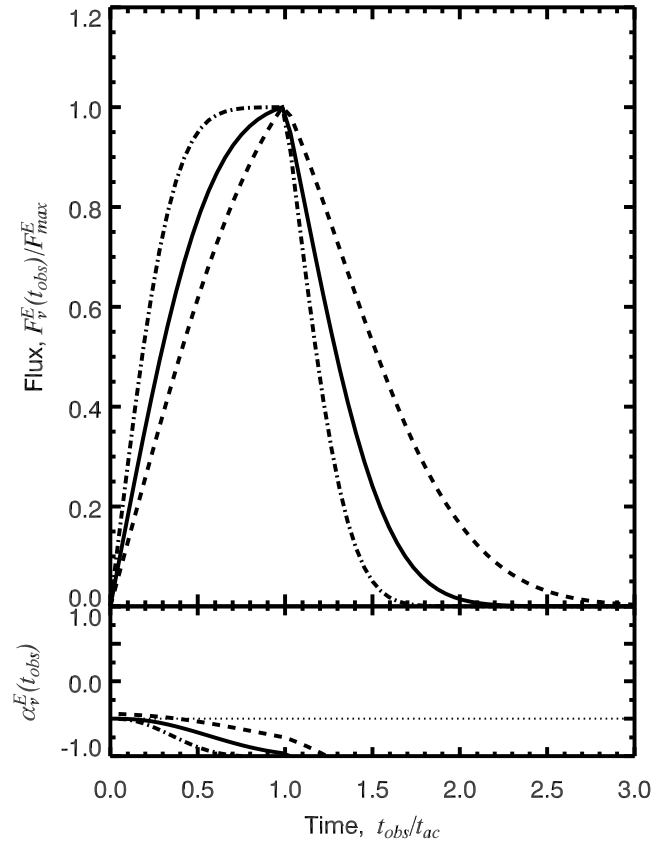


Fig. 6.— The same as Fig. 5 but for $\gamma_{min} = 10$.

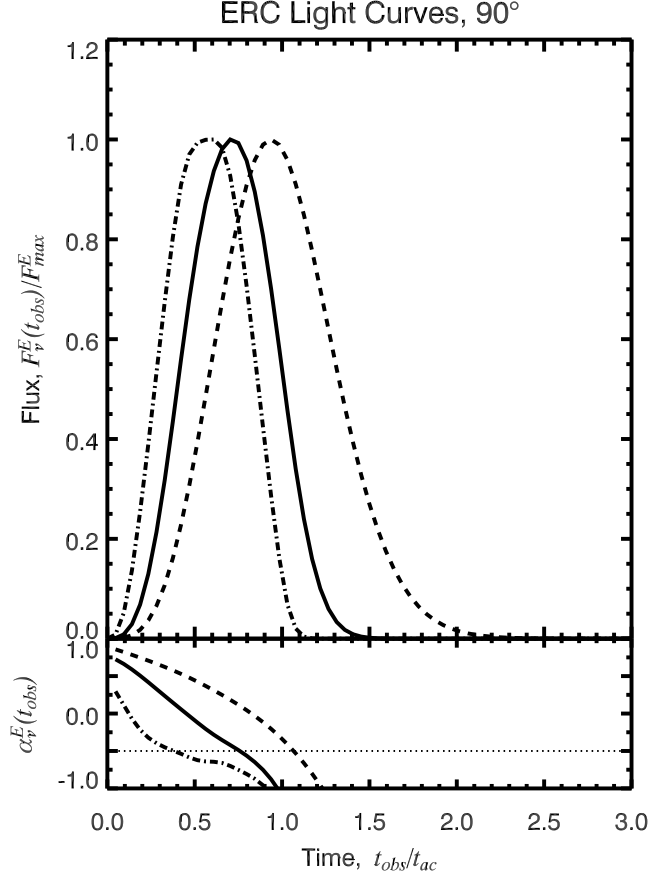


Fig. 7.— Normalized external Compton light curves for viewing angle $\theta_{obs} = 90^\circ$, $\theta'_{obs} = \sin^{-1}(1/\Gamma'_p)$, at frequencies of 10^{17} Hz (dashed), 4×10^{17} Hz (solid), and 2.5×10^{18} Hz (dot-dashed). The time dependence of the spectral index for each light curve is shown in the lower panel.

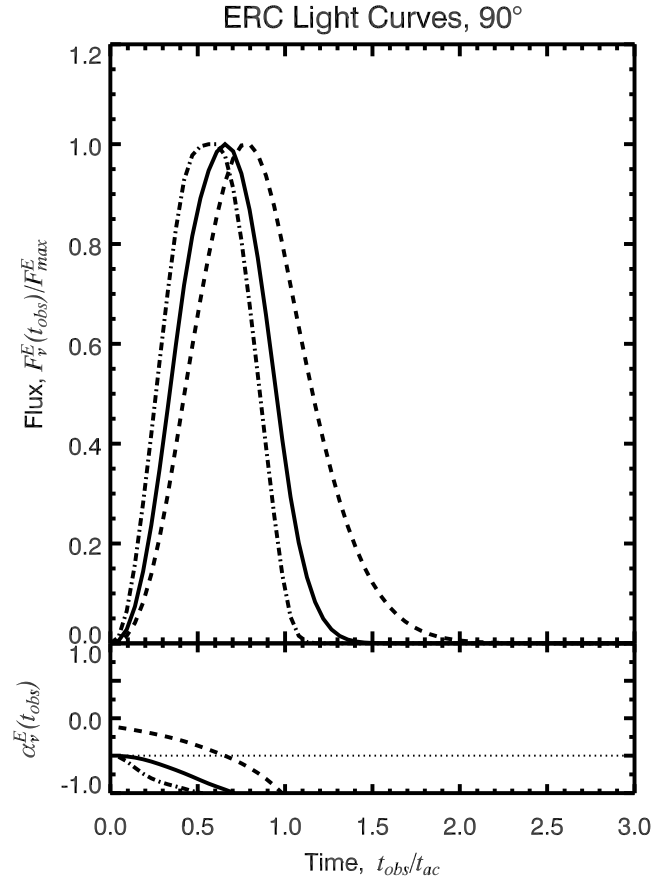


Fig. 8.— The same as Fig. 7 but for $\gamma_{min} = 10$.

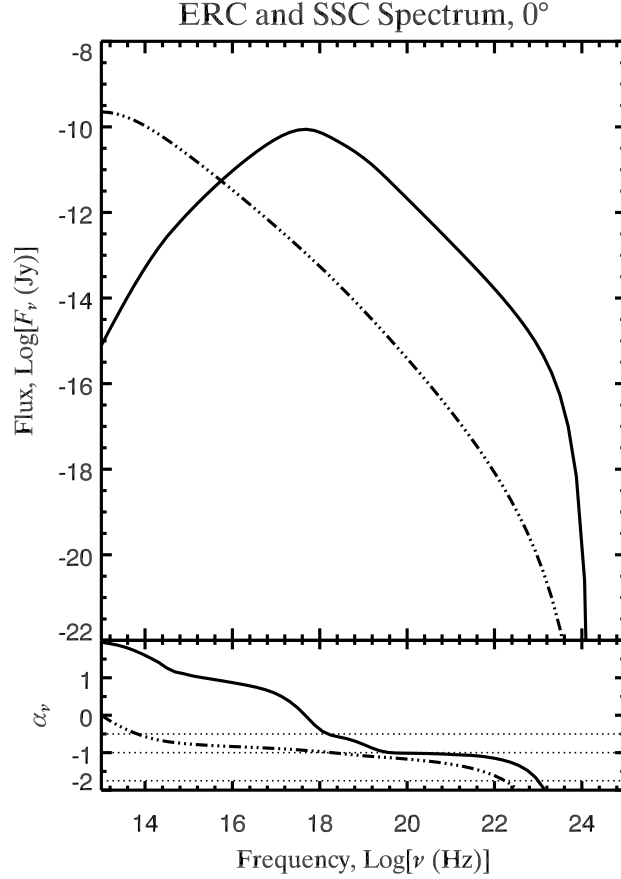


Fig. 9.— Synchrotron self-Compton (triple-dot-dashed curve) and external Compton (solid curve) spectrum for $\theta_{obs} = 0^\circ$ at the crossing time, $t = t_{ac}$. The emitting plasma is described by the same input parameters as in Fig. 3, while the parameters for the torus are the same as in Fig. 2, model (3). ERC radiation dominates over SSC radiation at frequencies above 10^{16} Hz. The SSC spectrum is different from the one presented in Paper I because the parameters have been chosen such that the electron energy losses are dominated by ERC emission (see Fig. 2).

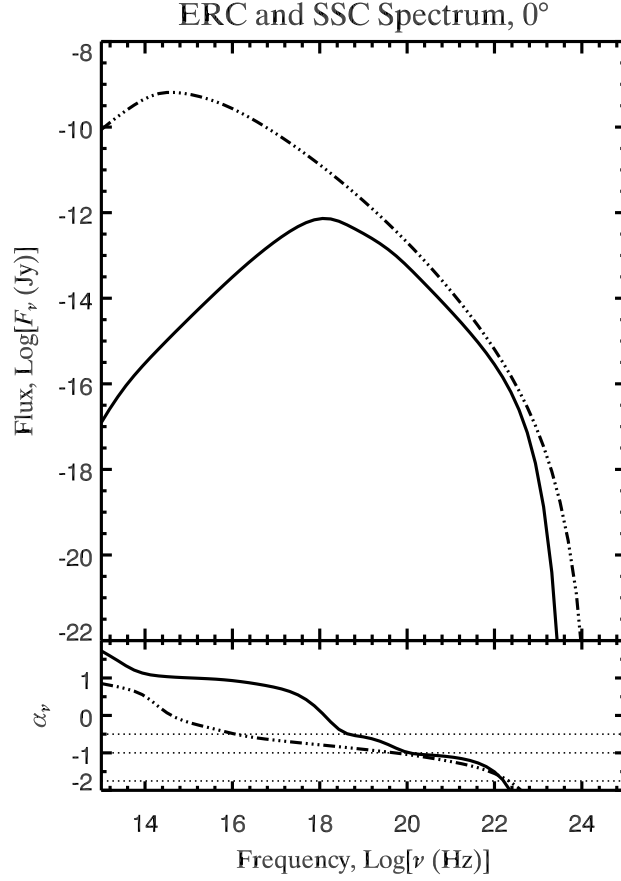


Fig. 10.— Same as Fig. 9 except that the parameters are set such that synchrotron self-Compton emission (triple-dot-dashed curve) dominates over ERC radiation (solid curve). Here the torus is assumed to be smaller and colder ($T = 800$ K, $r_{tor} = 7.0$ pc) while the emitting plasma is located at $z_p = 15$ pc. The plasma input parameters are the same as in Fig. 3.

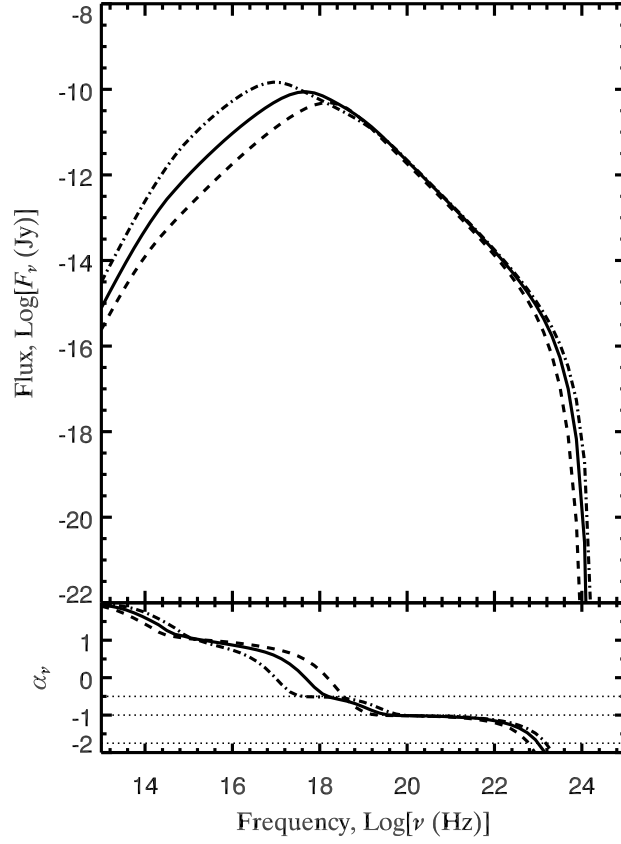


Fig. 11.— The dependence of the ERC spectrum on the bulk Lorentz factor of the emitting plasma (dot-dashed, solid, and dashed curves for $\Gamma'_p = 5, 10, 20$, respectively) when ERC losses of electrons provide the dominant energy loss mechanism. The input parameters are the same as in Fig. 3 except for Γ'_p .